SAND2016-0536C

Field Demonstration of the Sandia Wake Imaging System Capabilities at the Scaled Wind Farm Technology Facility

Thomas Herges[1], Randal Schmitt[2], David Bossert[3], Mark Johnson[4], Andres Sanchez[5], Crystal Glen[6], David Maniaci[7], and Brian Naughton[8]
Sandia National Laboratories, Albuquerque, NM, 87185

The Sandia Wake Imaging System is being developed to improve the capability of velocity measurements within the inflow and wake of wind turbines. The Doppler Global Velocimetry method has been selected for use by the Sandia Wake Imaging System for its ability to scale to large fields of view while still capturing instantaneous coherent structures, or velocity images, of the flowfield. The system allows improved spatial and temporal resolution capabilities for the purpose of validating high-fidelity models. The present work details a demonstration field test that measured the inflow velocity over a 3.5 m × 3.5 m viewing area at the Scaled Wind Farm Technology facility, which is operated by Sandia National Laboratories through U.S. Department of Energy funding. The goal of the field test was to demonstrate the application of Doppler Global Velocimetry safely at large outdoor scales. Measurements at these scales create new technical and safety issues, including outdoor laser propagation and aerosol particulate generation. These issues have been overcome to produce novel flow measurements that follow the same trends as the predicted measurements using a previously calibrated radiometric model.

Nomenclature

Δf_D = Doppler shift frequency
$\hat{\boldsymbol{i}}$ = incident unit vector
$\hat{\boldsymbol{o}}$ = observation unit vector
u = streamwise velocity coordinate (southerly direction)
V = velocity component along direction of velocity sensitivity
v = transverse velocity coordinate (easterly direction)
w = wall-normal velocity coordinate
x = streamwise spatial coordinate (southerly direction)
y = transverse spatial coordinate (easterly direction)
z = wall-normal spatial coordinate
v_{neq} = noise equivalent velocity
λ = laser wavelength

[1] Senior Member of the Technical Staff, Wind Energy Technologies Department, P.O. Box 5800.
[2] Principal Member of the Technical Staff, Laser, Optics and Remote Sensing Department, P.O. Box 5800.
[3] Principal Member of the Technical Staff, Optics and Sensor Engineering Department, P.O. Box 5800.
[4] Distinguished Technologist, Laser, Optics and Remote Sensing Department, P.O. Box 5800.
[5] Member of the Technical Staff, Contraband Detection Department, P.O. Box 5800.
[6] Manager, Laser, Optics and Remote Sensing Department, P.O. Box 5800.
[7] Senior Member of the Technical Staff, Wind Energy Technologies Department, P.O. Box 5800.
[8] Senior Member of the Technical Staff, Wind Energy Technologies Department, P.O. Box 5800.
Sandia National Laboratories is a multi-program laboratory managed and operated by Sandia Corporation, a wholly owned subsidiary of Lockheed Martin Corporation, for the U.S. Department of Energy's National Nuclear Security Administration under contract DE-AC04-94AL85000.

I. Introduction

Current wind turbine and wind farm models fail to reliably predict wind farm performance due to a lack of understanding in the fundamental physics involved in the interaction between complex atmospheric flow structures and wind turbines. This lack of understanding leads to uncertainty in optimizing wind farm design and layout for both power production and turbine lifetime [1-9]. Improved comprehension of the relevant flow physics through experimental measurements of wind turbine inflow and wakes can improve computational models through validation [10]. Scanning lidar [11-15], radar [4, 16-18], and particle image velocimetry (PIV) [9, 19, 20] have been shown to be promising non-intrusive velocity measurement technologies. Lidar and radar have produced novel measurements of the wind velocity and turbulence statics for multiple components at relatively short time scales over a large area near utility scale wind turbines and throughout wind farms [15, 18]. However, lidar and radar instrumentation are limited in their capability to instantaneously acquire coherent turbulent structures at short spatial and temporal scales [4, 11]. Alternatively, instantaneous turbulent coherent structures can be captured by PIV, but scaling PIV to large fields of view is extremely challenging since individual particles need to be resolved by the imaging device [21-25]. The scales of PIV are more suitable for wind tunnel applications and too limited without the use of extremely large tracer particles and impractical working distances for wind turbine investigations even with use of state-of-the-art cameras and lasers.

The present work details the demonstration field test of the Sandia Wake Imaging System (SWIS) at the Scaled Wind Farm Technology (SWiFT) facility [26], which is operated by Sandia National Laboratories through U.S. Department of Energy funding. This work is the continuation of previous developmental work to improve velocity measurement capabilities within the inflow and wake of wind turbines. Using the imaging area as an indicator of the measurement scale, the initial laboratory experiments were conducted on a 15 cm × 15 cm viewing area, followed by an intermediate-scale experiment with a 2 m × 2 m viewing area [27]. Presently, the field of view is a 3.5 m × 3.5 m area centered at a height of 9.8 m from the ground. This field test was the first deployment of the SWIS at scales relevant to testing at the SWiFT facility. The primary objective of the test was to safely demonstrate operation of the system (both laser and aerosol generation system) at large outdoor scales and acquire atmospheric boundary layer inflow velocity images. The velocity images have also been compared with secondary sonic anemometer measurements, in addition to simulated measurements of the SWIS using the previously calibrated radiometric model [27]. The radiometric model provided velocity measurement noise estimates for experimental planning and assessment prior to system deployment. The comparison of the simulated and experimental field measurements will help improve the system modeling capabilities leading to reduced velocity measurement uncertainty for future test campaign planning.

II. System Configuration

The velocimetry method chosen for use by the SWIS is Doppler Global Velocimetry (DGV), also referred to as Planar Doppler Velocimetry (PDV). The DGV diagnostic was selected as a best fit for the field measurement objectives and is more suited for large area measurements of instantaneous coherent turbulent structures [28-30]. DGV measures the Doppler shift frequency (Eq. (1)) of light scattered from aerosol particles within a flowfield illuminated by a narrow linewidth laser sheet. In Eq. (1), Δf_D is the Doppler shift frequency, λ is the incident laser wavelength, $\hat{\boldsymbol{o}}$ and $\hat{\boldsymbol{i}}$ are the light-wave observation and incident unit vectors respectively, and $\vec{\boldsymbol{V}}$ is the flow velocity [28, 29].

$$\Delta f_D = \frac{1}{\lambda}(\hat{\boldsymbol{o}} - \hat{\boldsymbol{i}}) \cdot \vec{\boldsymbol{V}} \tag{1}$$

A molecular iodine absorption filter contained within an optical cell (glass cylinder with optical windows), converts the Doppler shift frequency into an intensity variation measureable by cameras to produce a velocity image [31, 32]. The Doppler shift of the seeded particles is calculated at each pixel of the imaging device using Eq. (1), the measured intensity and camera observation unit vector, the iodine transmission profile, and the incident light-sheet-laser frequency and unit vector [32].

The SWIS configuration operated during the demonstration SWiFT inflow field test is shown in Figs. 1 and 2. The major system components include a narrow-linewidth laser, two intensified cameras (the receiver), and an aerosol generation system. The laser system was secured within a transportainer situated on a trailer while the receiver was housed in a specially modified field-test van. The field-test van was located downstream of the transportainer and measurement field of view located within the laser sheet. The aerosol generation system was attached to a boom lift positioned upstream of the measurement area. Both the transportainer and field-test van were

temperature controlled to maintain equipment stability and minimize signal drift, a challenging problem during field testing. A 10-meter-tall mobile metrology tower positioned near the viewing region recorded secondary velocity measurements with a sonic anemometer and the aerosol particulate concentration and size distribution using an aerodynamic particle sizer (APS). The mobile met tower is shown in Fig. 2.

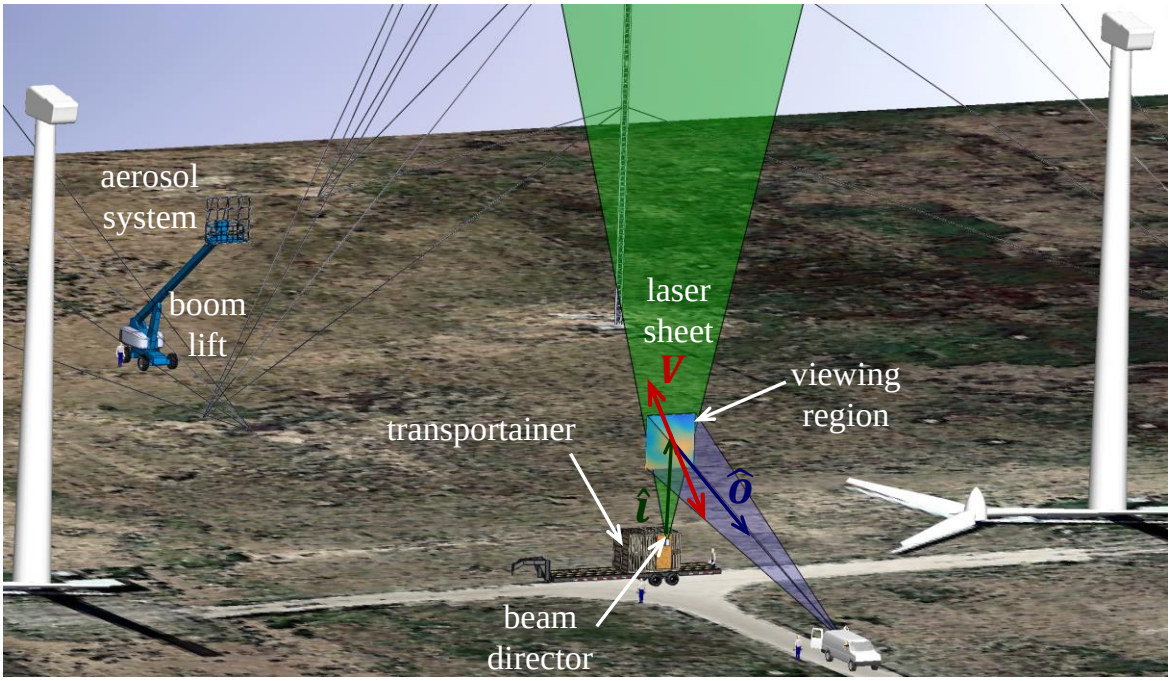

Figure 1. Schematic of the SWIS setup during the demonstration field test at SWiFT.

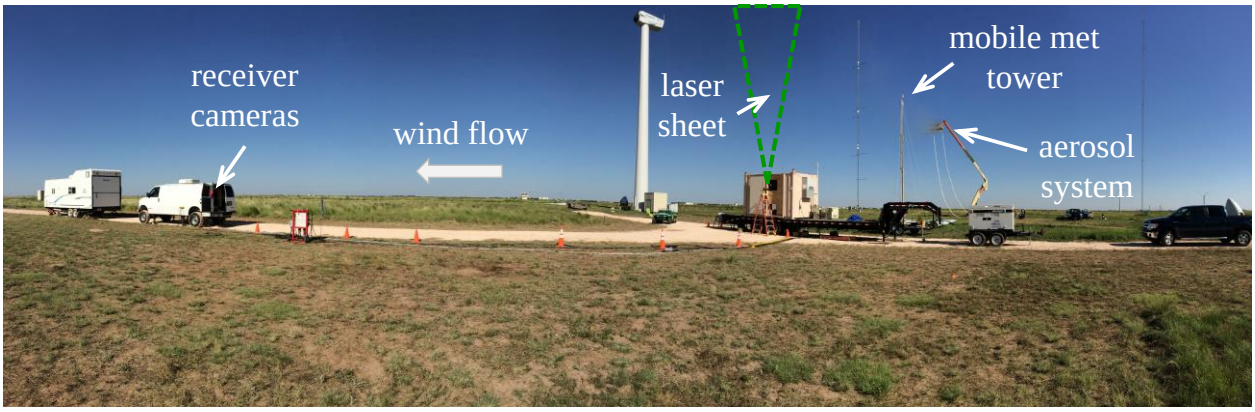

Figure 2. SWIS system components as deployed at the SWiFT facility in July 2015.

The SWIS measured the inflow velocity along the component indicated in Fig. 1 as V, with unit vector ($\boldsymbol{u} = 0.591$, $\boldsymbol{v} = .014$, $\boldsymbol{w} = -0.801$), where $\boldsymbol{u}$, $\boldsymbol{v}$, and $\boldsymbol{w}$ were the streamwise (southerly direction), transverse (easterly direction), and vertical directions, respectively. The spatial coordinates of ($\boldsymbol{x}$, $\boldsymbol{y}$, $\boldsymbol{z}$) correspond to the velocity components ($\boldsymbol{u}$, $\boldsymbol{v}$, $\boldsymbol{w}$). The measured velocity component was the result of the system layout and the Doppler shift equation, Eq. (1), where the bisector angle between the observation and incident laser light unit vector ($\hat{\boldsymbol{o}} - \hat{\boldsymbol{i}}$) defines the direction of the velocity sensitivity. The observation and incident laser light unit vectors vary slightly across the viewing region. The pixel-by-pixel unit vector variation was measured using an optical registration target attached to a boom lift. The spatial location of each registration dot was measured using a piece of surveying equipment called a total station (Fig. 3a). The boom-lift target also acted as a laser target (along with a laser plumb bob) to align the laser sheet vertically and measure the laser sheet's position and incident laser light unit vector using the total station (Fig. 3b).

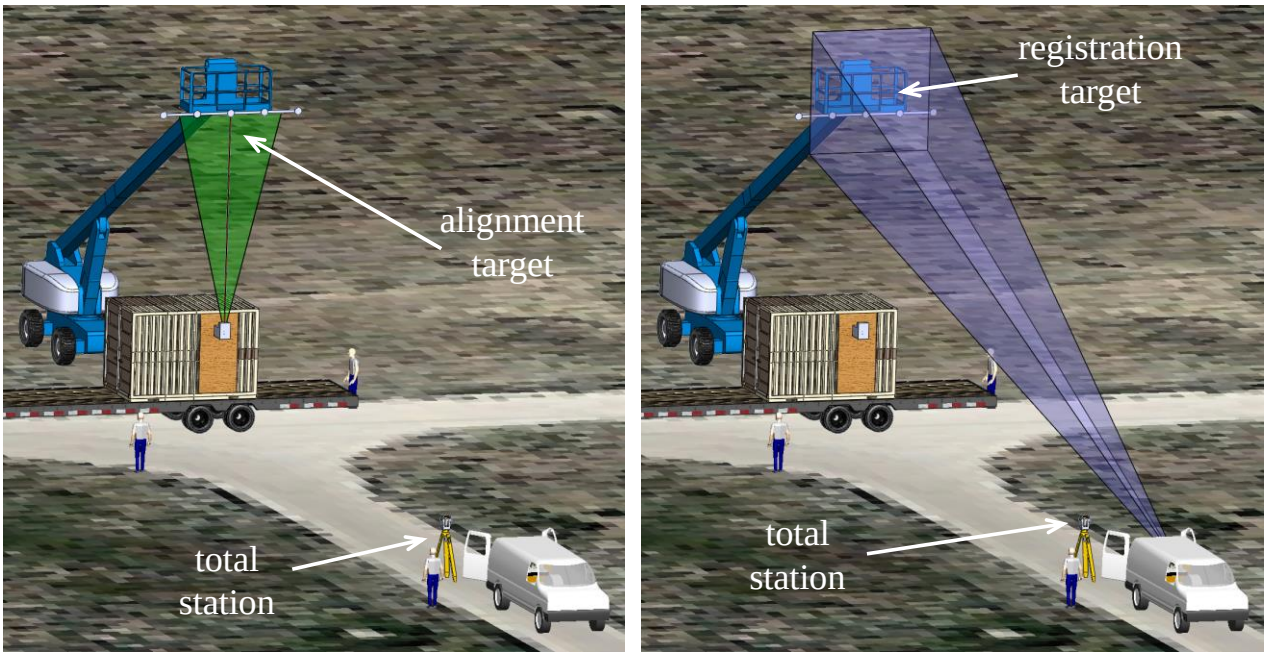

Figure 3. Schematic of the SWIS setup procedure: (a) laser sheet alignment and (b) image registration.

Scene illumination for the SWIS was provided by a narrow linewidth, frequency stabilized, laser transmission system located within the transportainer. Outdoor laser propagation of a class 4 laser creates safety challenges that require coordination with the Federal Aviation Administration (FAA) and U.S. Air Force Space Command Laser Clearinghouse. Details about the laser pointing accuracy, beam divergence, power output, and operation were shared with these agencies to avoid any airspace conflicts within the nominal laser hazard zone. In addition, two visual observers were used to ensure that aircraft, wildlife, and debris did not enter the nominal laser hazard zone during outdoor laser propagation.

Most of the laser energy was steered out of the transportainer through a beam director that formed the laser into a 1-cm-thick vertical light sheet. The mirrors and cylindrical lens located within the beam director set the laser sheet half-angle divergence to 18.5 degrees, while the exit aperture cut the half-angle divergence to 13.7 degrees for outdoor laser propagation. At the beam director exit, the laser power was approximately 300 mJ per pulse. A small portion of the laser output was used to monitor the frequency of the laser with a reference iodine cell and phototubes. This information was used to correct for frequency drift of the laser during data collection. The laser system used during field testing is thoroughly described by Herges et al [27].

The receiver system, which consisted of two intensified charge-coupled device (ICCD) cameras with 100-mm-fl f/2 lenses, a large aperture iodine vapor cell, a 50/50 beamsplitter, a 0.4 transmittance neutral density (ND) filter, and a turning mirror, imaged the light sheet over a 3.5 m × 3.5 m viewing region at a height of 9.8 m. The 5-centimeter-diameter iodine cell was placed in front of the lens on one of the ICCD cameras (signal camera), acting as a filter that converted changes in optical frequency (due to the Doppler shift from scattering particles) to changes in intensity. The second ICCD camera was used as a reference camera so that variations in laser illumination and/or variations in the aerosol density could be removed through ratioing images. A 50/50 beamsplitter was used to combine the line-of-sight of both cameras so they could record images without parallax. A neutral density filter (ND) with 0.4 transmittance was placed in front of the reference camera to match the losses through the iodine cell and iodine-cell housing of the signal camera optical path. The final pointing mirror allowed fine adjustment of the signal and reference camera viewing regions when collecting data in the field. Both ICCD cameras included narrow bandpass filters centered at 532 nm and infrared (IR) blocking filters to eliminate background light. The receiver assembly was built on a removable breadboard to allow alignment and characterizations in the laboratory before deployment in the back of the customized field-test van. The ICCD cameras, built by Andor Technologies, have 512 × 512 CCD sensors and Gen III image intensifiers. For these experiments, the receiver was positioned 27 m from the light sheet, to yield the 3.5 m × 3.5 m field of view. During data acquisition, on-chip 2 × 2, 4 × 4, and 8 × 8 pixel binning was used to record images with 256 × 256, 128 × 128, and 64 × 64 pixels corresponding to a ~1.5 cm, ~3 cm, and ~6 cm spatial resolution (at the laser sheet). The primary pixel binning used was a 4 × 4

binning. Pixel binning increases the scattering signal intensity per pixel, improving the signal-to-noise ratio, and acts as a low-pass spatial filter. The images may be further binned through software methods during analysis if needed. The data were processed offline using the MATLAB code and the iodine line characterized in Ref. [27].

A. Aerosol System

The aerosol particles were introduced to increase the signal levels of scattered laser light sensed by the receiver cameras. The aerosol generation system consisted of 20 spray nozzles (4 rows of 5 nozzles) arranged on a 3.048 m × 3.048 m aluminum frame and connected to the front of the aerial boom lift platform (Fig. 4). The spray nozzles produced a mist of potassium chloride (KCl)/water solution. The KCl particles were chosen because they are safe and easy to generate in large amounts outdoors and are also effective in providing sufficient laser light scatter. The distance between the aerosol generation system and the measurement region was primarily to allow the dispersion of the aerosol particles to cover the field of view, while also providing sufficient time for the liquid to completely evaporate, leaving small KCl particles entrained in the atmospheric boundary layer. The direction and height of the aerosol system was dependent on wind speed and direction throughout the day. The air pressure for the nozzle system was supplied by a diesel air compressor at 65 psi with a liquid flow rate of 3.83 liters per minute (LPM) per nozzle. Optimal salt-water concentration was determined to be 10g/L (KCl/tap water), producing a particle-laden stream of liquid droplet aerosols with an approximate size of ~13 μm. The droplets dried out as they moved downstream, producing a ~1.3 μm-diameter polydispersed size distribution of crystalline KCl particles. Electrical power for this system was supplied with a portable diesel electrical generator.

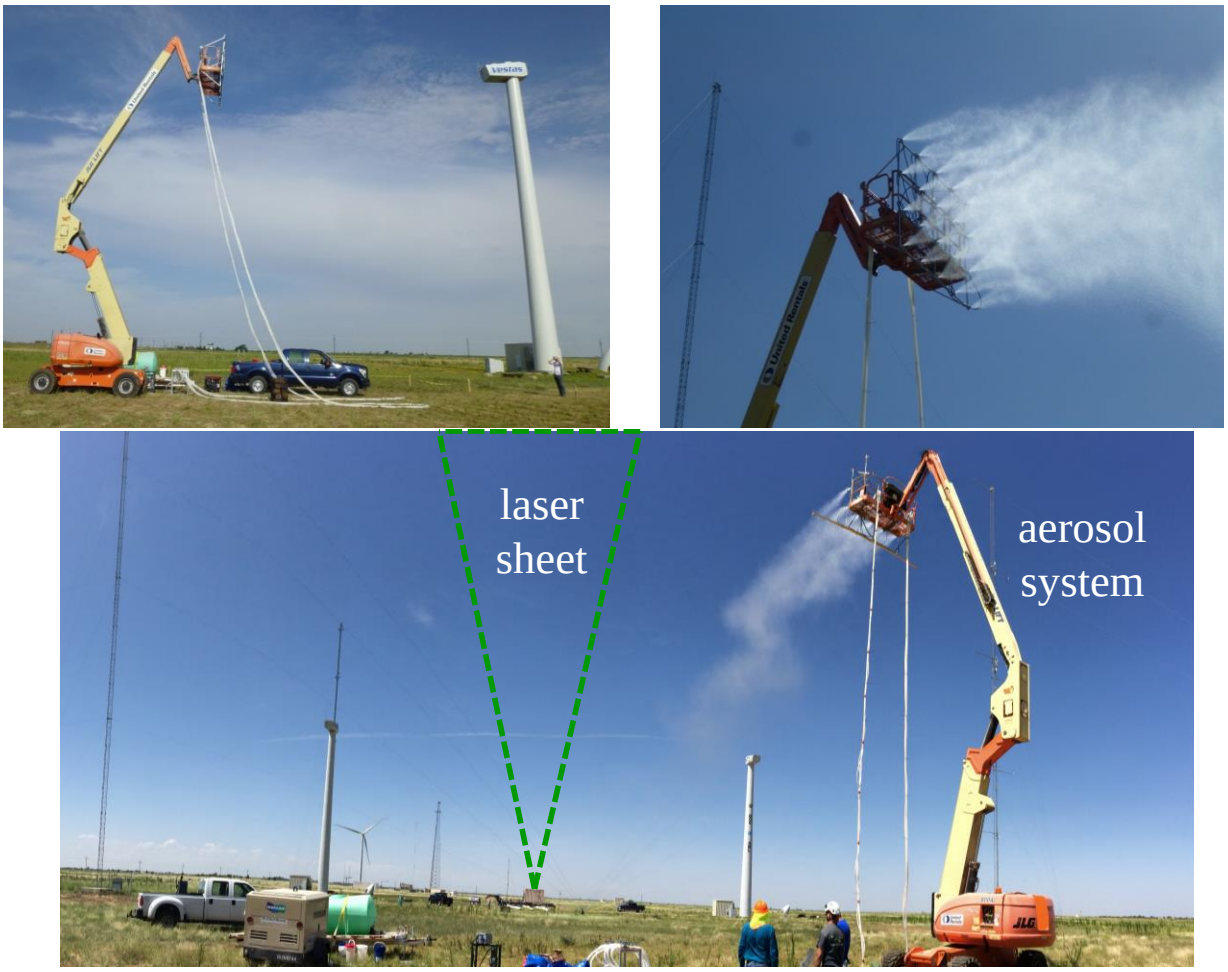

Figure 4. Aerosol generation system during the SWIS demonstration field test.

III. Demonstration Field Test Results

A. Aerosol System

SWIS data was acquired on July 15th and 16th, 2015 using the generated KCl particulates and background (naturally occurring, "native aerosol") particulates, respectively. An aerosol particulate measurements system, or aerodynamic particle sizer (APS), was used to collect particle concentrations during the field test. The APS was placed on top of the transportainer during the measurement period at an approximate height of 5.5 m from the ground. The KCl mist had drying issues due to a higher humidity than anticipated during testing. The drying issue required that the aerosol system be positioned further upstream (approximately 90 m from the measurement area) in order to have dry KCl aerosol particulates downstream at the transportainer. A combination of the increased distance between the aerosol system and the measurement region, the area that the aerosol plume covered, and the meandering of the plume within the atmospheric boundary layer (observed in Fig. 4) resulted in a hit (aerosol particulates observed by the receiver) percentage of 28% in the acquired images. The aerosol plume was visually observed to fluctuate the full distance between the turbine towers (~90m) in a short amount of time (within minutes) with a southerly wind highlighting the challenge of positioning a plume far downwind.

Figures 5 and 6 show the total aerosol particulate concentration sampled by the APS on July 15th (KCl aerosol generation system) and July 16th (background aerosol particulates), respectively.

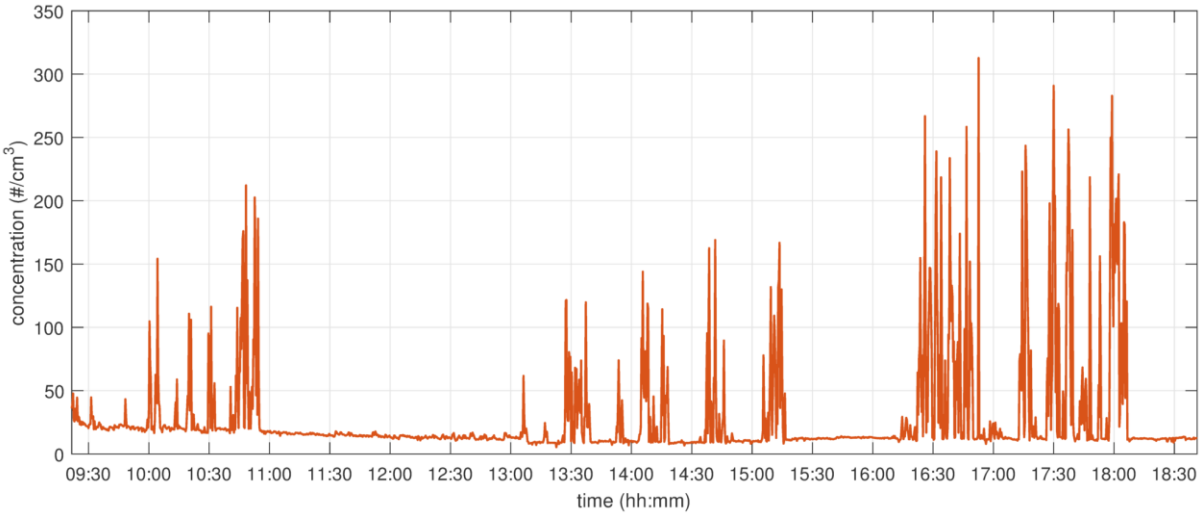

Figure 5. KCl aerosol plume concentration vs time on July 15th, 2015.

Figure 6. Background aerosol concentration vs time on July16th, 2015.

The average background (native aerosol) concentration for July 15th was calculated at 13.7 #/cm^3. Plume concentrations were dependent on a few factors: wind speed, sampler placement, and solution concentration. It is important to note that the first two plume groups, seen in Fig. 5, were disseminated with an approximate salt-water concentration of 11.32 g/L and the last plume group was disseminated with an approximate salt-water concentration of 13.66 g/L using different potassium chloride powders. This difference in solution concentration may account for the slightly higher concentrations in the last plume set. The average wind speed for July 16th was 4.4 m/s at a height of 10 m, while the average background concentration of the native aerosol was 13.16 #/cm^3.

Isokinetic sampling of the aerosol plume would have been preferred for the APS measurements at a position closer to the viewing region due to the variations in the wind speed. Additionally, the concentration measurements of the KCl plume were likely biased to lower levels due to the low hit percentage of the plume at the APS, the long 20 s sample time, and the lower background aerosol concentrations.

B. Simulated Velocity Measurement Predictions

Comparing simulated velocity measurements with demonstration field test velocity measurements helps improve system modelling leading to reduced velocity measurement uncertainty and improved system capabilities for future experimental planning. The performance of the Sandia Wake Imaging System (SWIS) is most simply represented in a single metric called noise equivalent velocity (v_{neq}). Noise equivalent velocity is determined by the conversion of the primary noise sources in the receiver cameras during the measurement into a velocity value that is added randomly to the true velocity value. The metric provides a value for comparing relative measurement uncertainties between configuration options, but the v_{neq} calculation only includes the dominant sources of measurement uncertainty and is not the total velocity measurement uncertainty of the system. Ideally, the v_{neq} value is zero, but in reality it is determined by the hardware and experimental conditions.

The dominant noise sources in the SWIS include shot noise of the signal photons, camera read noise, and excess noise from the intensifier gain. Other uncertainty sources include iodine cell calibration [33], spatially varying laser frequency [28, 30, 34, 35], iodine filter temperature sensitivities [28], and background light [36]. However, these other uncertainty sources primarily contribute to a systematic bias uncertainty and are not included in the model used for the current velocity measurement predictions of the Sandia Wake Imaging System. The measurements from the previous scaling experiment also revealed that the shot noise signal photons were likely correlated between the signal and reference cameras in the final velocity calculation [27]. The shot noise of the signal photons equals the square root of the number of photoelectrons collected per binned pixel, so the noise equivalent velocity from shot noise at the receiver depends inversely on the number of photoelectrons collected. Thus, the noise equivalent velocity from shot noise can be reduced if the number of photoelectrons match pixel-by-pixel between the signal and reference cameras, explaining why the ND filter was added to the optical path of the reference camera. Even though the ND filter reduced the number of photoelectrons acquired by the reference camera, the overall noise in the velocity measurement was reduced due to the shot noise (photoelectron count) being more closely correlated between the signal and reference cameras.

A computational model of the SWIS has been developed to predict and optimize the performance of the system using different equipment configurations. The SWIS model was calibrated using the data from the previous scaling and sensitivity field test [27]. During the previous test, the system sensitivity limits were analyzed by varying the aerosol concentration in a zero-velocity flowfield and measuring the corresponding signal levels on the receiver as shown in Fig. 7a. The number of photons collected at the receiver was calculated from the analog-to-digital (A/D) counts measured by the cameras using the Andor-supplied sensitivity specifications and correlated with measured aerosol concentration. The data in Fig. 7a were used to calibrate the differential scattering cross section value of the aerosol particulates. In addition to the particulate differential scattering cross section, the SWIS computation model incorporates the three-dimensional system layout, a pin-hole camera model [37-40] to account for the camera stand-off distance and perspective, receiver lens aperture size, laser energy with a super Gaussian laser intensity profile, laser sheet divergence, and aerosol concentration. The variation in differential scattering cross section with scattering angle was accounted for in the SWIS model through a Mie scattering simulation using the previously measured particle size distribution for KCl [27]. The model computes the ideal measurement of an input representative flowfield of interest and superimposes the calculated noise equivalent velocity (v_{neq}) from the radiometric model on a pixel-by-pixel basis since the noise equivalent velocity varies across the viewing area.

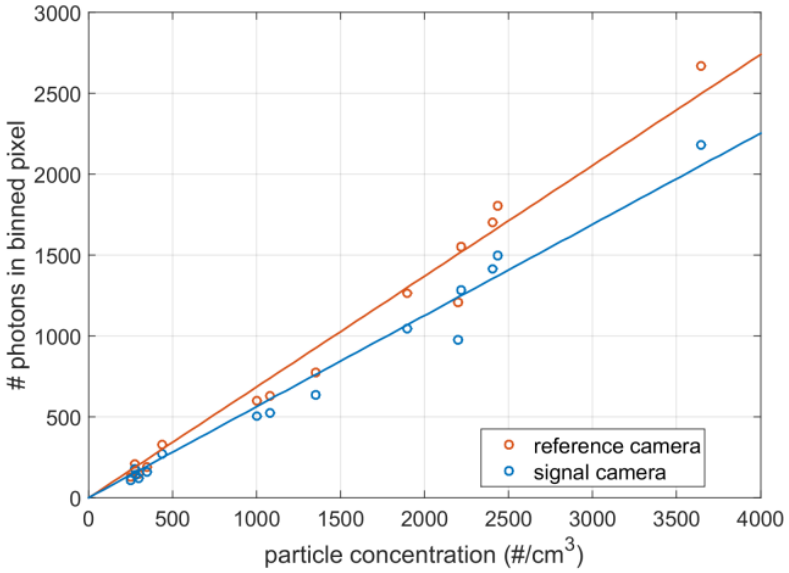

Figure 7. Number of photons collected at the receiver versus the aerosol particulate concentration [27].

The simulated velocity measurements were made using a representative flowfield of the atmospheric boundary layer inflow. The representative atmospheric boundary layer displayed in Fig. 8 was modeled using the Mann model incorporated into the WAsP IEC Turbulence Simulator [41, 42]. Fig. 8 displays the representative flowfield where $\boldsymbol{u}$ is the streamwise (southerly direction, Fig. 8a), $\boldsymbol{v}$ is the transverse (easterly direction, Fig. 8b), and $\boldsymbol{w}$ is the vertical direction (Fig. 8c).

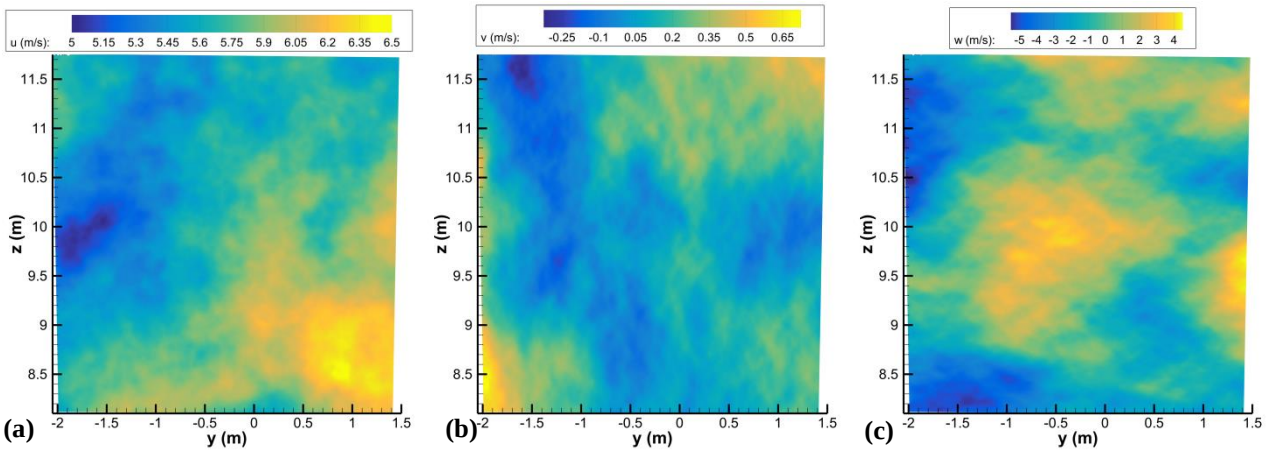

Figure 8. Representative simulated atmospheric boundary layer inflow: (a) u velocity component, (b) v velocity component, and (c) w velocity component.

Figure 9 presents simulated velocity measurements of the representative atmospheric boundary layer inflow with different ICCD camera pixel binning and aerosol particulate concentrations. The corresponding noise equivalent velocities are summarized in Table 1. Aerosol particulate concentrations of 300 #/cm^3 (Figs. 9a, 9c, and 9d) and 13 #/cm^3 (Figs. 9b and 9d) were used to match the concentrations measured on July 15th using the generated KCl particulates (Fig. 5) and July 16th background (naturally occurring, "native aerosol") particulates (Fig. 6), respectively. Additionally, simulations used 2 × 2 (Fig. 9e), 4 × 4 (Figs. 9a and 9b), and 8 × 8 (Figs. 9c and 9d) pixel binning to match the binning settings used during the field test measurements. The perfect, or ideal, velocity measurement is displayed in Fig. 9f.

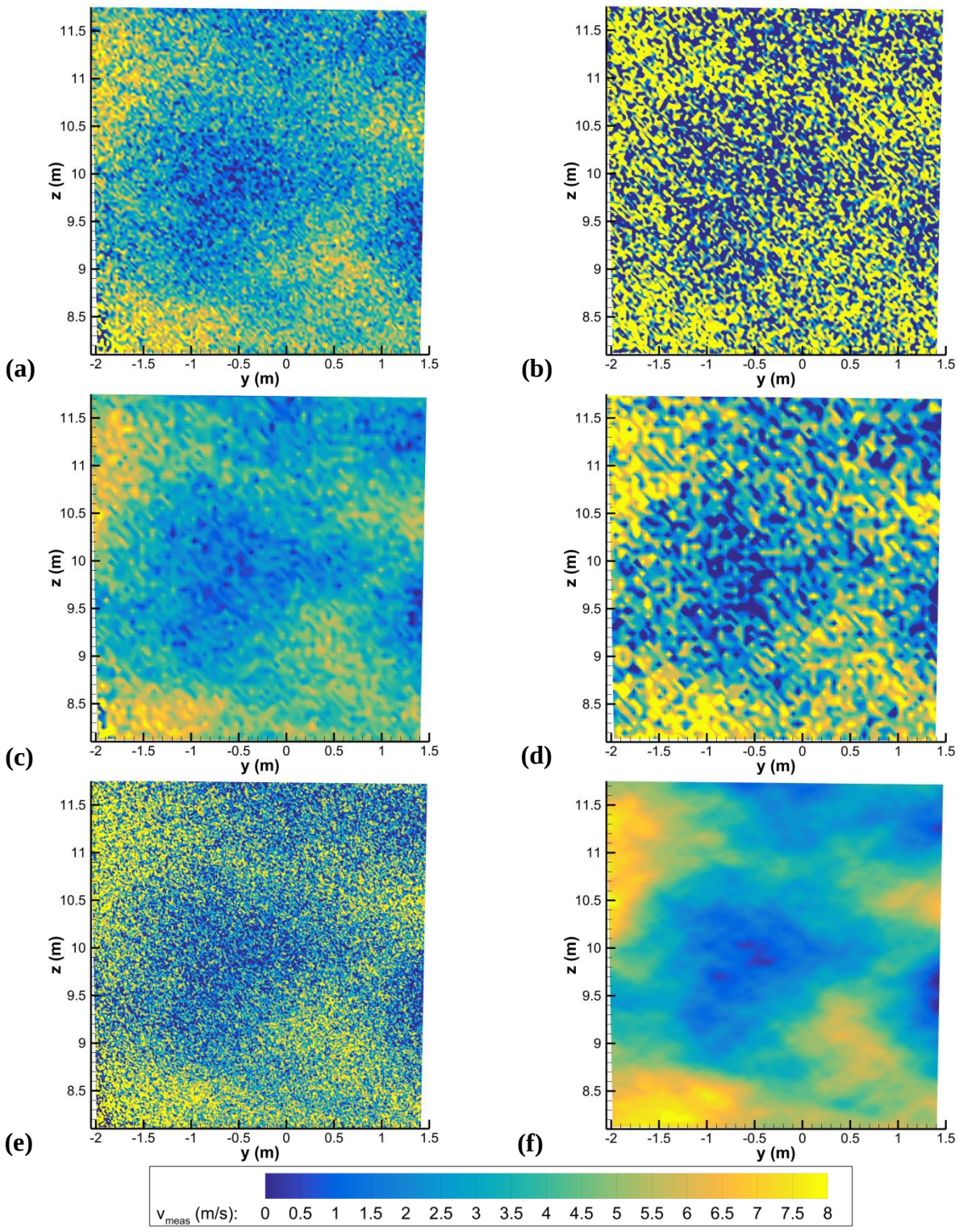

Figure 9. Simulated velocity measurements of representative flowfield using the SWIS radiometric model: (a) 4 × 4 binning with 300 #/cm^3 particulate concentration (v_{neq} = ±2.39m/s), (b) 4 × 4 binning with 13 #/cm^3 particulate concentration (v_{neq} = ±13.13 m/s), (c) 8 × 8 binning with 300 #/cm^3 particulate concentration (v_{neq} = ±1.18 m/s), (d) 8 × 8 binning with 13 #/cm^3 particulate concentration (v_{neq} = ±5.91 m/s), (e) 2 × 2 binning with 300 #/cm^3 particulate concentration (v_{neq} = ±4.88 m/s), and (f) ideal velocity measurement.

Figure 9 and Table 1 show that as the aerosol particulate concentration increases, the scattering intensity acquired by the receiver increases, reducing the noise in the velocity measurement. The measurement predictions also reveal that aerosol seeding augmenting the background aerosol particulates is required to acquire velocity measurements without excessive noise corruption. At higher concentrations, v_{neq} is reduced by a factor of two for each level of additional binning because the dominate measurement noise source in the DGV system is shot noise in the photons. The velocity measurements are said to be shot-noise limited. As a result, each binning of pixels (2×2) increases the signal by a factor of 4 and the signal-to-noise ratio (SNR) by a factor of 2, reducing the noise equivalent velocity by a factor of 2. Increasing the camera binning from 4×4 to 8×8 while using lower particulate concentrations, reduces the v_{neq} by a factor greater than two (Figs. 9b and 9d) due to the presence of read noise. The low photon signal levels observed at 13 #/cm^3 increases the impact of read noise on the velocity measurement. Therefore, the velocity measurement is not shot-noise limited at low particulate concentration levels even though shot noise is still the dominate noise source. Many of the flow structures in the atmospheric boundary layer are still resolved with decreased spatial resolution using 8×8 binning (Fig. 9c).

Table 1: Summarized Simulated SWIS Velocity Measurements

pixel binning	concentration (#/cm^3)	average noise equivalent velocity, v_{neq} (m/s)	Figure
4×4	300	±2.39	9a
4×4	13	±13.13	9b
8×8	300	±1.18	9c
8×8	13	±5.91	9d
2×2	300	±4.88	9e

C. Velocity Measurements

Figure 10 shows velocity images acquired using both KCl aerosol generation (Figs. 10a, 10c, and 10e) and background aerosols (Figs. 10b and 10d). The elevation angle of the receiver was about 17 degrees for the as-deployed SWIS field test configuration. The component of the measured velocity was 59.1% of the streamwise component (southerly), 80.1% of the vertical component, and 1.4% of the component parallel to the laser sheet (easterly). The reduced amount of scatted light acquired only using background aerosols increases the observed velocity noise (Figs. 10b and 10d) as predicted in the simulated velocity measurements (Figs. 9b and 9d). The velocity images acquired using generated KCl particulates appear to show flow structures near the edges of the viewing area and laser sheet. These flow structures are most likely the result of variation in particulate concentration rather than actual measured velocity gradients. Velocity gradients near the center of the image are likely due to velocity variations in the atmospheric boundary layer. Areas of increased noise in the velocity images correlate with regions of reduced particulate concentration.

The average velocity images for each data set, example presented in Fig. 11, were used to remove the observed spatial frequency variation in the laser sheet as well as the bullseye-fringe pattern created from the windows of the iodine cell. The averaged velocity images were used because a more preferable zero-velocity image could not be acquired due to the constant wind conditions. As a result, the images (Fig. 10) and velocity traces (Fig. 12) show the velocity change (Δv) relative to the average acquired over a data set, or 133 seconds (1 data set was 2000 images acquired at 15 Hz) rather than an absolute velocity measurement. A new, more frequently stable pulse-burst laser designed specifically for the SWIS and improved iodine cell windows could overcome this deficiency and allow the acquisition of the absolute velocity images without the need of a zero-velocity wind condition.

A region of the SWIS velocity images matching the spatial resolution of the mobile met tower sonic anemometer was sampled to produce the comparative velocity traces for the SWIS and sonic anemometer displayed in Fig. 12. The three-component sonic anemometer data has been transformed to match the measured velocity component of the SWIS acquired at the same sample rate (15 Hz). The velocity traces were additionally processed to display the change in velocity, with the average velocity over 133 s subtracted. The SWIS-calculated velocity data captured without a sufficient KCl plume have been removed from the velocity traces in Figs. 12a, 12c, and 12e, corresponding to hit percentages (aerosol particulates observed by the receiver) of 28%, 7%, and 28%, respectively.

Table 2 lists the standard deviation of the velocity measured by the sonic anemometer and the SWIS for the velocity images and traces in Figs. 10 and 12. The sonic anemometer velocity standard deviation varied between ±0.66 - ±1.07. However, during KCl operation the SWIS velocity trace standard deviation remained constant. Note

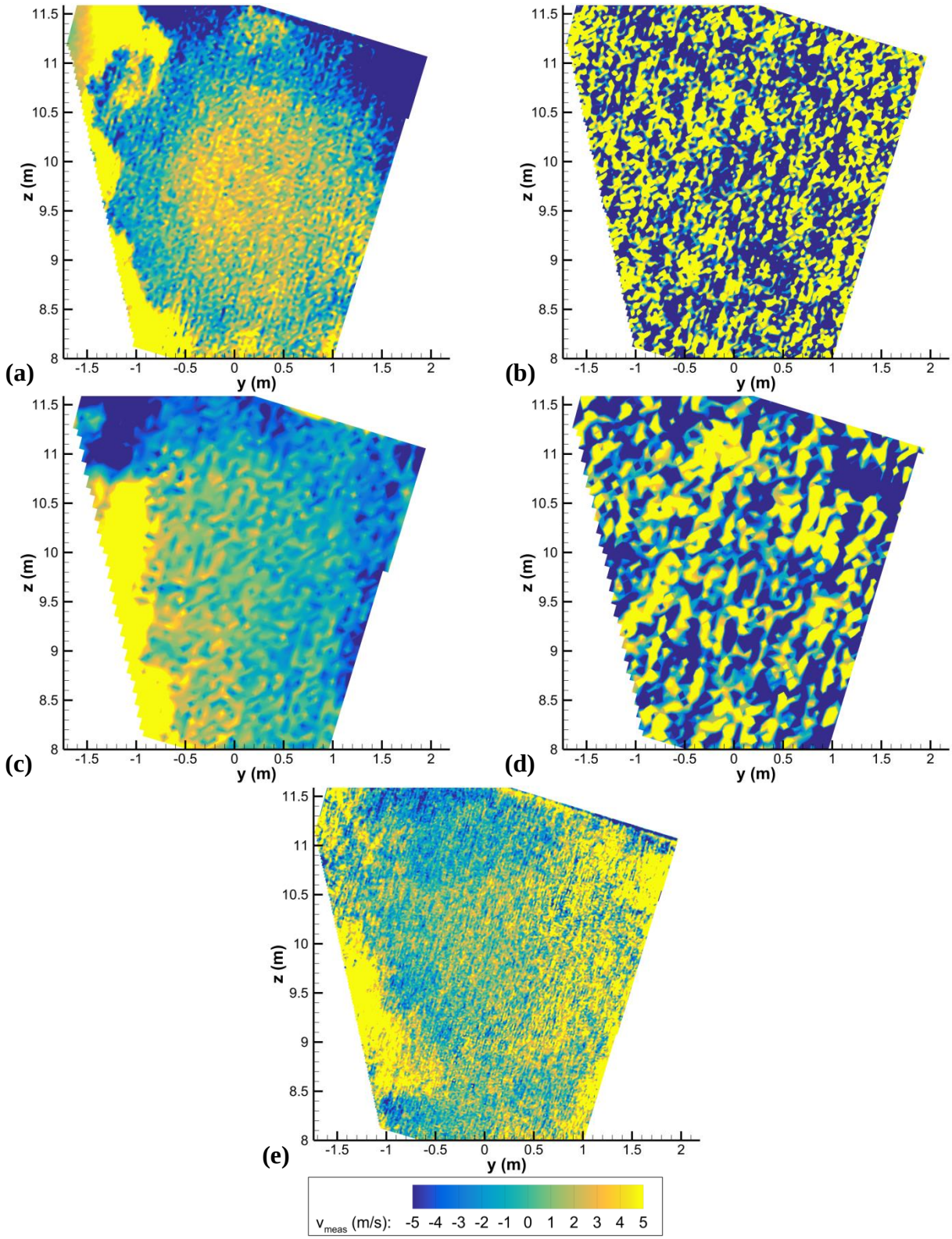

Figure 10. Velocity images acquired by the SWIS: (a) 4 × 4 binning with KCL aerosol generation (b) 4 × 4 binning with background aerosol particulates, (c) 8 × 8 binning with KCL aerosol generation, (d) 8 × 8 binning with background aerosol particulates, and (e) 2 × 2 binning with KCL aerosol generation.

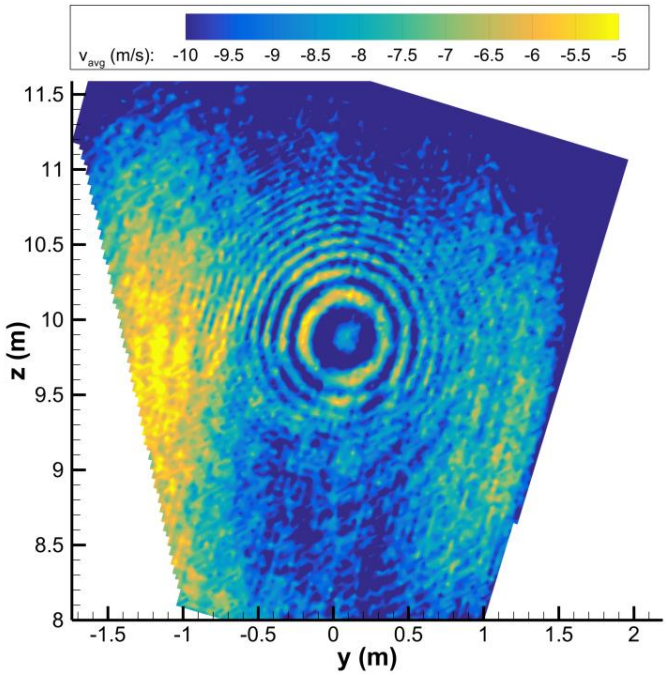

Figure 11. Example average velocity images acquired by the SWIS.

that the same area was sampled across all cases (meaning lower pixel binning averaged more pixels). Table 2 also presents the time and date of the measurement, an estimate on the average particulate concentration sampled by the APS during the data set, and the percentage of frames with adequate seeding (hit percentage). The standard deviation in velocity at each pixel was calculated using the frames with sufficient seeding. A region of interest near the center of the images was used to calculate the average standard deviation in velocity for each pixel, with the results included in Table 2.

Table 2: Summarized SWIS Measurement Results

pixel binning	APS measurement (#/cm^3)	date/time	$v_{\text{sonic,std}}$ (m/s)	$v_{\text{SWIS,std}}$ (m/s)	$v_{\text{pixel,std}}$ (m/s)	hit percentage
4 × 4	50.8	15-Jul-2015 15:09:19	±0.99	±1.26	±3.24	0.28
4 × 4	13.6	16-Jul-2015 09:35:02	±0.66	±5.78	±15.77	--
8 × 8	102.0	15-Jul-2015 16:37:59	±0.86	±1.26	±1.26	0.07
8 × 8	14.0	16-Jul-2015 09:31:22	±0.90	±2.46	±8.55	--
2 × 2	82.5	15-Jul-2015 17:14:19	±1.07	±1.25	±4.16	0.28

The $v_{\text{pixel,std}}$ results are most analogous to the noise equivalent velocity predictions in the previous section and show the same trend as the simulated measurements (Table 3). A zero-velocity measurement would have allowed a more direct comparison between the $v_{\text{pixel,std}}$ (measured) and the v_{neq} (simulated) data. Drawing conclusions from the measured SWIS Δv standard deviation results by comparing binning and particulate concentrations cases is difficult due to the changing wind conditions between data sets and particulate concentration uncertainty in the viewing area. The velocity standard deviation is reduced with increased aerosol concentration and increased pixel binning. Velocity fluctuations in the wind velocity and aerosol concentration are included in the $v_{\text{pixel,std}}$ measurements unlike the v_{neq} estimates. Thus, the $v_{\text{pixel,std}}$ are similar but consistently higher than the simulated noise equivalent velocity results. Additionally, the factor in standard deviation between the $v_{\text{pixel,std}}$ cases and the factor in noise between the v_{neq} cases are not equal. The similarity between the measurements and predictions helps improve confidence in the SWIS model for planning future test campaigns that will be needed to validate high-fidelity models.

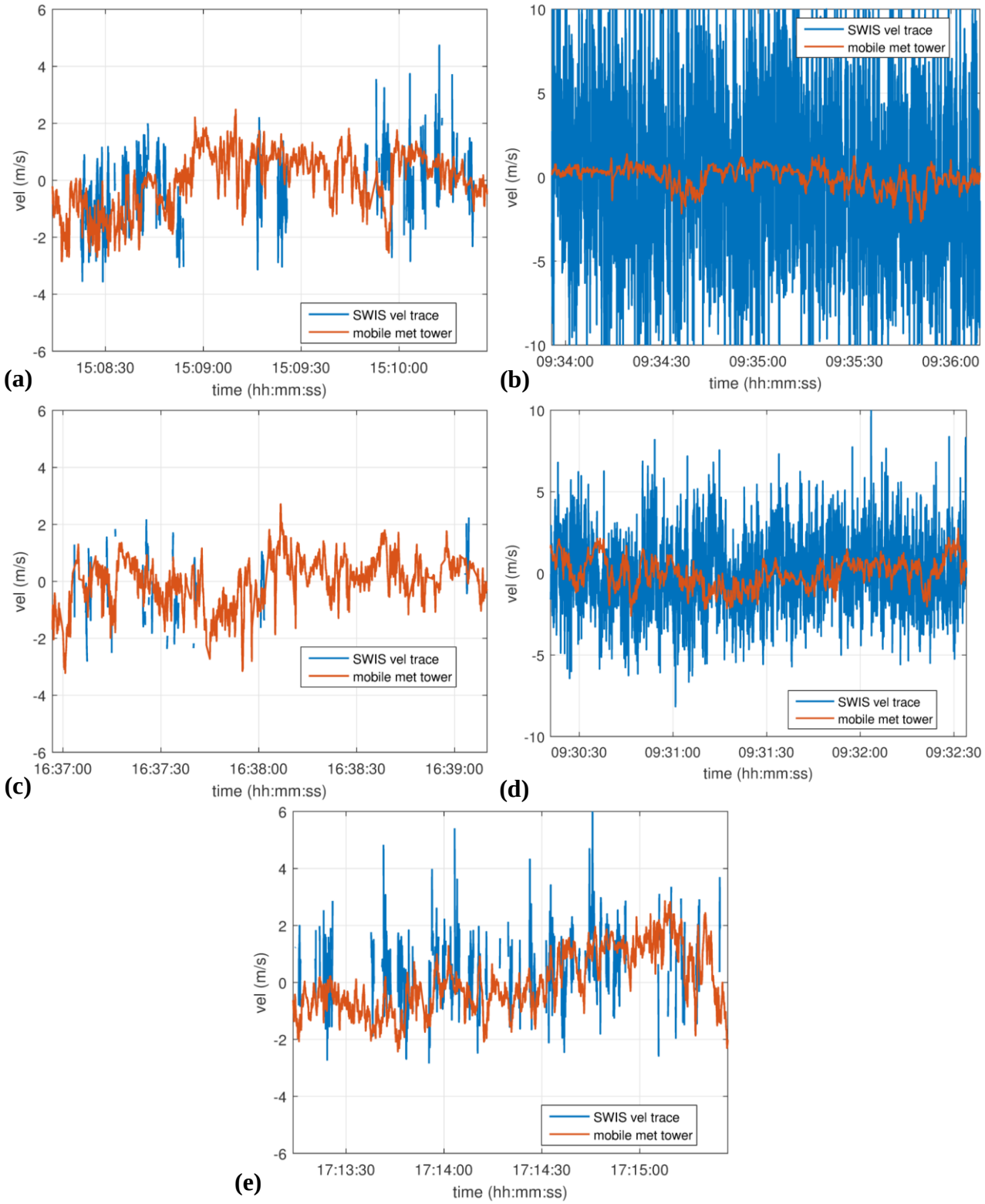

Figure 12. Velocity trace comparison between sample SWIS region and mobile met tower sonic anemometer: (a) 4 × 4 binning with KCL aerosol generation (b) 4 × 4 binning with background aerosol particulates, (c) 8 × 8 binning with KCL aerosol generation, (d) 8 × 8 binning with background aerosol particulates, and (e) 2 × 2 binning with KCL aerosol generation.

Table 3: SWIS Measurement and Simulated Measurement Comparison

pixel binning	APS measurement (#/cm^3)	$v_{\text{pixel,std}}$ (m/s)	simulated concentration (#/cm^3)	v_{neq} (m/s)
4 × 4	50.8	±3.24	300	±2.39
4 × 4	13.6	±15.77	13	±13.13
8 × 8	102.0	±1.26	300	±1.18
8 × 8	14.0	±8.55	13	±5.91
2 × 2	82.5	±4.16	300	±4.88

IV. Conclusions

The Sandia Wake Imaging System (SWIS) uses the Doppler Global Velocimetry (DGV) technique to acquire instantaneous velocity images within an outdoor laser sheet projected over a large field of view. DGV was chosen due to its ability to capture instantaneous velocity fields and flow structures with improved scaling capabilities compared to other velocity diagnostics. The current work details the demonstration field test of the SWIS to safely measure the incoming atmospheric boundary layer at the Scaled Wind Farm Technology (SWiFT) facility. This field test was a demonstration of DGV outdoors and over larger fields of view than previously achieved. A measurement of the change in a single velocity component relative to the average over a 3.5 m × 3.5 m viewing area centered at a height of 9.8 m was obtained. Comparison of the SWIS velocity measurements with an independent sonic anemometer showed noisier velocity measurements with higher standard deviations. Conversely, the measurements agreed well with simulated measurements of the system using a previous calibrated radiometric model of the SWIS. This result improves confidence in the radiometric model which will be used for future experimental planning and system development needed to validate high-fidelity models. System improvements, such as a new pulse-burst laser, modified iodine cell, and an adjusted aerosol generation system with a larger coverage area, will allow absolute velocity measurements with reduced noise and reduced nominal ocular hazard distance in the airspace above the measurement. The SWIS velocity measurements will complement lidar and radar velocity measurements within wind farms and in the vicinity of wind turbines to acquire the high-resolution data necessary for validating of high-fidelity modeling codes.

Acknowledgments

This work was funded by the US Department of Energy Wind and Water Power Technologies Office. In addition to our DOE sponsors, the authors would like to acknowledge our fellow Sandia National Laboratories colleague Alice Sobczak for her ongoing technical contribution to the project and the Sandia Wind Energy Technologies Department summer interns, Phillip Chui, Khuong Nguyen, Rachel Meyer, and Hales Swift, whom provided a valuable service as visual observers during the field test. Additionally, we thank Carsten Westergaard of NextraTEC and James Meyers of NASA Langley Research Center for providing expert technical advice, historical perspective, and extensive technical discussions that have significantly benefited the project.

References

1. Barthelmie, R. J., Hansen, K., Frandsen, S. T., Rathmann, O., Schepers, J. G., Schlez, W., Phillips, J., Rados, K., Zervos, A., Politis, E. S., and Chaviaropoulos, P. K. "Modelling and measuring flow and wind turbine wakes in large wind farms offshore," *Wind Energy* Vol. 12, No. 5, 2009, pp. 431-444. doi: 10.1002/we.348
2. Barthelmie, R. J., Frandsen, S. T., Nielsen, M. N., Pryor, S. C., Rethore, P. E., and Jørgensen, H. E. "Modelling and measurements of power losses and turbulence intensity in wind turbine wakes at Middelgrunden offshore wind farm," *Wind Energy* Vol. 10, No. 6, 2007, pp. 517-528. doi: 10.1002/we.238
3. Sherry, M., Nemes, A., Lo Jacono, D., Blackburn, H. M., and Sheridan, J. "The interaction of helical tip and root vortices in a wind turbine wake," *Physics of Fluids* Vol. 25, No. 11, 2013, pp. -. doi: 10.1063/1.4824734
4. Hirth, B. D., Schroeder, J. L., Gunter, W. S., and Guynes, J. G. "Coupling Doppler radar-derived wind maps with operational turbine data to document wind farm complex flows," *Wind Energy*, 2014, pp. n/a-n/a. doi: 10.1002/we.1701

5. Barthelmie, R. J., Pryor, S. C., Frandsen, S. T., Hansen, K. S., Schepers, J. G., Rados, K., Schlez, W., Neubert, A., Jensen, L. E., and Neckelmann, S. "Quantifying the Impact of Wind Turbine Wakes on Power Output at Offshore Wind Farms," *Journal of Atmospheric and Oceanic Technology* Vol. 27, No. 8, 2010, pp. 1302-1317. doi: 10.1175/2010JTECHA1398.1
6. Barthelmie, R. J., and Jensen, L. E. "Evaluation of wind farm efficiency and wind turbine wakes at the Nysted offshore wind farm," *Wind Energy* Vol. 13, No. 6, 2010, pp. 573-586. doi: 10.1002/we.408
7. McKay, P., Carriveau, R., and Ting, D. S. K. "Wake impacts on downstream wind turbine performance and yaw alignment," *Wind Energy* Vol. 16, No. 2, 2013, pp. 221-234. doi: 10.1002/we.544
8. Hansen, K. S., Barthelmie, R. J., Jensen, L. E., and Sommer, A. "The impact of turbulence intensity and atmospheric stability on power deficits due to wind turbine wakes at Horns Rev wind farm," *Wind Energy* Vol. 15, No. 1, 2012, pp. 183-196. doi: 10.1002/we.512
9. Hong, J., Toloui, M., Chamorro, L. P., Guala, M., Howard, K., Riley, S., Tucker, J., and Sotiropoulos, F. "Natural snowfall reveals large-scale flow structures in the wake of a 2.5-MW wind turbine," *Nature Communications* Vol. 5, 2014. doi: 10.1038/ncomms5216
10. Naughton, J. "Instrumentation and Test Facility Needs for Wind Turbine Technology Development," *50th AIAA Aerospace Sciences Meeting including the New Horizons Forum and Aerospace Exposition*. American Institute of Aeronautics and Astronautics, 2012.
11. Sjöholm, M., Angelou, N., Hansen, P., Hansen, K. H., Mikkelsen, T., Haga, S., Silgjerd, J. A., and Starsmore, N. "Two-Dimensional Rotorcraft Downwash Flow Field Measurements by Lidar-Based Wind Scanners with Agile Beam Steering," *Journal of Atmospheric and Oceanic Technology* Vol. 31, No. 4, 2013, pp. 930-937. doi: 10.1175/JTECH-D-13-00010.1
12. Bingöl, F., Mann, J., and Larsen, G. C. "Light detection and ranging measurements of wake dynamics part I: one-dimensional scanning," *Wind Energy* Vol. 13, No. 1, 2010, pp. 51-61. doi: 10.1002/we.352
13. Trujillo, J.-J., Bingöl, F., Larsen, G. C., Mann, J., and Kühn, M. "Light detection and ranging measurements of wake dynamics. Part II: two-dimensional scanning," *Wind Energy* Vol. 14, No. 1, 2011, pp. 61-75. doi: 10.1002/we.402
14. Iungo, G. V., and Porté-Agel, F. "Volumetric scans of wind turbine wakes performed with three simultaneous wind LiDARs under different atmospheric stability regimes," *Journal of Physics: Conference Series* Vol. 524, No. 1, 2014, p. 012164.
15. Angelou, N., and Sjöholm, M. "UniTTe WP3/MC1: Measuring the inflow towards a Nordtank 500kW turbine using three short-range WindScanners and one SpinnerLidar." DTU Wind Energy, 2015.
16. Hirth, B. D., and Schroeder, J. L. "Documenting Wind Speed and Power Deficits behind a Utility-Scale Wind Turbine," *Journal of Applied Meteorology and Climatology* Vol. 52, No. 1, 2012, pp. 39-46. doi: 10.1175/JAMC-D-12-0145.1
17. Hirth, B. D., Schroeder, J. L., Gunter, W. S., and Guynes, J. G. "Measuring a Utility-Scale Turbine Wake Using the TTUKa Mobile Research Radars," *Journal of Atmospheric and Oceanic Technology* Vol. 29, No. 6, 2012, pp. 765-771. doi: 10.1175/JTECH-D-12-00039.1
18. Marathe, N., Swift, A., Hirth, B., Walker, R., and Schroeder, J. "Characterizing power performance and wake of a wind turbine under yaw and blade pitch," *Wind Energy*, 2015. doi: 10.1002/we.1875
19. Toloui, M., Riley, S., Hong, J., Howard, K., Chamorro, L. P., Guala, M., and Tucker, J. "Measurement of atmospheric boundary layer based on super-large-scale particle image velocimetry using natural snowfall," *Experiments in Fluids* Vol. 55, No. 5, 2014, pp. 1-14. doi: 10.1007/s00348-014-1737-1
20. Morris, S. C., Stolpa, S. R., Slaboch, P. E., and Klewicki, J. C. "Near-surface particle image velocimetry measurements in a transitionally rough-wall atmospheric boundary layer," *Journal of Fluid Mechanics* Vol. 580, 2007, pp. 319-338. doi: 10.1017/S0022112007005435
21. Adrian, R. J., and Westerweel, J. *Particle Image Velocimetry*: Cambridge University Press, 2011.
22. Scarano, F., and Westerweel, J. "Particle Image Velocimetry," *Springer Handbook of Experimental Fluid Mechanics*. Springer, 2007, pp. 309-342.
23. Pol, S. U., and Balakumar, B. J. "Design considerations for large field particle image velocimetery (LF-PIV)," *Measurement Science and Technology* Vol. 24, No. 2, 2013, p. 025302.
24. Bosbach, J., Kühn, M., and Wagner, C. "Large scale particle image velocimetry with helium filled soap bubbles," *Experiments in Fluids* Vol. 46, No. 3, 2009, pp. 539-547. doi: 10.1007/s00348-008-0579-0
25. Scarano, F., Ghaemi, S., Caridi, G., Bosbach, J., Dierksheide, U., and Sciacchitano, A. "On the use of helium-filled soap bubbles for large-scale Tomographic PIV wind tunnel experiments," *13th International Symposium on Applications of Laser Techniques to Fluid Mechanics*. Lisbon, Portugal, 2014.

26. Berg, J., Bryant, J., LeBlanc, B., Maniaci, D. C., Naughton, B., Paquette, J. A., Resor, B. R., White, J., and Kroeker, D. "Scaled Wind Farm Technology Facility Overview," *32nd ASME Wind Energy Symposium*. American Institute of Aeronautics and Astronautics, 2014.
27. Herges, T., Bossert, D., Schmitt, R., Glen, C., Maniaci, D. C., and Naughton, B. "Preliminary Field Test of the Wind Turbine Wake Imaging System," *33rd Wind Energy Symposium*, 2015.
doi: 10.2514/6.2015-0219
28. Meyers, J. F., Lee, J. W., and Cavone, A. A. "Doppler Global Velocimetry," *Springer Handbook of Experimental Fluid Mechanics*. Springer, 2007, pp. 342-353.
29. Meyers, J. F., Lee, J. W., and Schwartz, R. J. "Characterization of measurement error sources in Doppler global velocimetry," *Measurement Science and Technology* Vol. 12, 2001, pp. 357-368.
30. McKenzie, R. L. "Measurement capabilities of planar Doppler velocimetry using pulsed lasers," *Applied Optics* Vol. 35, No. 6, 1996, pp. 948-964.
doi: 10.1364/AO.35.000948
31. Elliott, G. S., and Beutner, T. J. "Molecular filter based planar Doppler velocimetry," *Progress in Aerospace Sciences* Vol. 35, No. 8, 1999, pp. 799-845.
doi: 10.1016/S0376-0421(99)00008-1
32. Mosedale, A. D., Elliott, G. S., Carter, C. D., and Beutner, T. J. "Planar Doppler Velocimetry in a Large-Scale Facility," *AIAA Journal* Vol. 38, No. 6, 2000, pp. 1010-1024.
doi: 10.2514/2.1085
33. Lee, J., and Meyers, J. "Increase Accuracy in Molecular Filter Based Flow Field Diagnostics Through Direct Frequency Calibration Using Optical Modulators," *43rd AIAA Aerospace Sciences Meeting and Exhibit*. American Institute of Aeronautics and Astronautics, 2005.
34. Forkey, J. N., Lempert, W. R., and Miles, R. B. "Observation of a 100-MHz frequency variation across the output of a frequency-doubled injection-seeded unstable-resonator Q-switched Nd:YAG laser," *Optics Letters* Vol. 22, No. 4, 1997, pp. 230-232.
doi: 10.1364/OL.22.000230
35. Morrison, G. L., and Suryanarayanan, S. "DGV's Accuracy Dependence Upon Laser Beam Intensity Profile," *ASME 2009 Fluids Engineering Division Summer Meeting*. FEDSM2009-78245, 2009.
36. Elliott, G. S., Crafton, J., Baust, H. D., Beutner, T. J., Carter, C. D., and Tyler, C. "Evaluation and Optimization of a Multi-component Planar Doppler Velocimetry System," *43rd AIAA Aerospace Sciences Metting*. Reno Nevada, 2005.
37. Willert, C. E. "Assessment of camera models for use in planar velocimetry calibration," *Experiments in Fluids* Vol. 41, No. 1, 2006, pp. 135-143.
doi: 10.1007/s00348-006-0165-2
38. Charrett, T. O. H., Nobes, D. S., and Tatam, R. P. "Investigation into the selection of viewing configurations for three-component planar Doppler velocimetry measurements," *Applied Optics* Vol. 46, No. 19, 2007, pp. 4102-4116.
doi: 10.1364/AO.46.004102
39. Nobes, D. S., Wieneke, B., and Tatam, R. P. "Determination of view vectors from image warping mapping functions," *Optical Engineering* Vol. 43, No. 2, 2004, pp. 407-414.
doi: 10.1117/1.1636765
40. Tsai, R. Y. "A versatile camera calibration technique for high-accuracy 3D machine vision metrology using off-the-shelf TV cameras and lenses," *Robotics and Automation, IEEE Journal of* Vol. 3, No. 4, 1987, pp. 323-344.
doi: 10.1109/JRA.1987.1087109
41. "IEC Turbulence Simulator." 2.00.0002 ed., 2015.
42. Mann, J. "The spectral velocity tensor in moderately complex terrain," *Journal of Wind Engineering and Industrial Aerodynamics* Vol. 88, No. 2–3, 2000, pp. 153-169.
doi: http://dx.doi.org/10.1016/S0167-6105(00)00046-5